Chapter 3

Wind and structural response

3.1 Introduction

Wind engineering has shown a clear advancement in the design of structures to synoptic winds after Alan G. Davenport's breakthrough framework of wind load estimation for structures through the famous Davenport chain in 1961. This framework was outlined considering synoptic winds in which the mean and fluctuating component of the wind speed can be separated through a time average of 10 minutes to 1 hour resulting in a constant mean and an approximately stationary Gaussian fluctuation. For many years, this has been the basis for the design criterion of wind in all codes of practice. Although small-scale wind events that form due to convective activities such as tornadoes and downbursts have resulted in devastating outcomes in previous years, contrary to synoptic winds, design guidelines that are collectively agreed upon by researchers are not available for these transient events. A downburst is one of the small-scale meteorological events in which a downdraft of air impinges on the earth's surface creating a radial outflow (Fujita, 1985). In the past 20 years researchers have been trying to simulate downburst winds in wind tunnels (Chay and Letchford, 2002; Junayed et al., 2019; Letchford et al., 2002; Mason et al., 2005; Romanic et al., 2019) and in the framework of computational fluid dynamics (CFD) (Aboshosha et al., 2015; Chay et al., 2006; Kim and Hangan, 2007; Sengupta et al., 2008; Vermeire et al., 2011). On the other hand, researchers also proposed and applied analytical methods for the estimation of wind response during downbursts (Chen and Letchford, 2004; Chen, 2008; Choi and Hidayat, 2002; Holmes et al., 2005; Kwon and Kareem, 2009; Roncallo and Solari, 2020; Solari et al., 2015a). However, the proposed simulations and analytical methods were not validated with full-scale wind and structural response measurements during a downburst. The need for full-scale monitoring is essential to check whether the simplifying assumptions considered in the proposed downburst wind load modeling are acceptable and to see if other

parameters have been given sufficient importance in the proposed models. There is a major advancement in the collection of downburst wind speed data through a network of closely spaced anemometers (Repetto et al., 2017; Solari et al., 2020), but the collection of simultaneous measurement of wind and structural response data is very rare.

In this chapter, the wind-induced response of the monitored structure introduced in Chapter 2 is studied using the full-scale wind and structural response registered during two downburst events. The relative simplicity of the structure in terms of structural properties and geometry makes it suitable for future validation studies. The procedure that has been followed to extract downburst events from the recorded wind data is described in Section 3.2. The selected case studies of downbursts along with the registered wind and structural response data are presented in Section 3.3. The wind and structural response data are discussed and analyzed in Section 3.4. Finally, conclusions are made and prospects for future research are recommended in Section 3.5.

3.2 Wind data and separation algorithm

The main objective of this research is to study the response of the structure during downburst events. Thus, detecting the time ranges in which downburst events have occurred is the first crucial step. Different approaches for the classification of wind events were adopted in various previous studies. Anemometric readings of wind speed and other meteorological indicators were used in some research (Cook et al., 2003; Huang et al., 2019; Lombardo et al., 2009; Twisdale and Vickery, 1992). Wind speed data has been used as the only basis for classification in Durañona et al. (2007) and De Gaetano et al. (2014). Wind speed data and detailed meteorological analysis were the basis of classification in Burlando et al. (2018). Since the monitored structure is not equipped with temperature, humidity, and atmospheric pressure sensors, a method proposed in De Gaetano et al. (2014) that uses wind speed data as a sole input for the classification of high-intensity winds into different categories was adopted. The classification is into three families defined in De Gaetano et al. (2014) as

1. stationary Gaussian events, with relatively large mean velocities and small gust factors; such events usually correspond to neutral synoptic atmospheric conditions; they are here referred to as ABL events

2. non-stationary non-Gaussian events, with large peak velocities and gust factors but relatively small mean velocities; they are herein referred to as thunderstorms

3. stationary non-Gaussian events, with relatively small mean velocities, abut large peaks and gust factors; they are here referred to as gust fronts

This classification method is based on the notable feature of thunderstorm winds in which a sudden increase and decrease in wind speed occur within a few minutes. This feature can be quantified using the gust factor, the ratio between the peak and the mean wind speed. Three gust factors defined in Eq. (3.1) were calculated for every instant of time at which the instantaneous wind speed value is greater than 15 m/s.

$$G_{60} = \frac{\hat{V}_{1s}}{\bar{V}_{60}} \qquad G_{10} = \frac{\hat{V}_{1s}}{\bar{V}_{10}} \qquad G_1 = \frac{\hat{V}_{1s}}{\bar{V}_1} \tag{3.1}$$

where G_{60}, G_{10}, and G_1 are 1-hr, 10-minute, and 1-minute gust factors respectively; $\bar{V}_{60}$, $\bar{V}_{10}$, and $\bar{V}_1$ are 1 hour, 10-minute and 1-minute averaged wind speeds respectively; and $\hat{V}_{1s}$ is peak wind speed averaged over 1 second. On the other hand, expected reference gust factors for an atmospheric boundary layer (ABL) wind at the height of the anemometer, G^0_{60}, G^0_{10}, G^0_1 , were calculated using ESDU (1984) and Solari (1993) taking into account the roughness at the site and the roughness changes upwind for every horizontal wind direction sector. The result is shown in Fig. 3.1. The calculated 1-hour and 10-minute gust factors, G_{60} and G_{10}, centered on every instant of time were compared with the expected gust factor for an ABL wind, G^0_{60} and G^0_{10}. A time instant at which the calculated gust factor falls outside a range of threshold of the expected gust factor for an ABL wind is classified as a time instant corresponding to thunder or gust phenomenon. The range of threshold for each of the expected gust factors is adopted from De Gaetano et al. (2014). In addition, a criterion based on the ratio of the 1-minute to 10-minute gust factor was also applied according to De Gaetano et al. (2014). The separation process and threshold criteria are summarized in Fig. 3.2. After every instant of time is labeled as either ABL or thunder/gust, thunder/gust instants are combined to form a single event provided that there is less than 4 hrs of a gap between them. On the other hand, ABL instants are combined to form a single depression event provided that the time gap between them is less than 72 hrs. Since the wind data acquired by the anemometers is at a sampling rate of 0.1 seconds, an automatic algorithm was written to implement this separation procedure with minimum time. The automatic algorithm identified 20 ABL events and 23 thunder or gust events. Once this quantitative separation is done, a qualitative separation is applied by visual inspection to classify the thunder/gust wind events into the category of downburst or gust front. Through visual inspection, only two possible downburst events were found out of the 23 possible thunder/gust events.

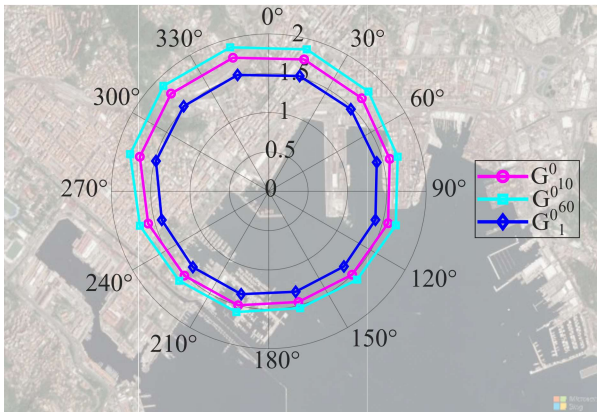

Fig. 3.1 Reference gust factor

3.3 Selected events wind records and structural response

3.3.1 Wind records

Two downburst events were selected through the procedure explained in section 3 to study the response of the structure. Fig. 3.3 shows 1 hour time history of instantaneous wind speed, V, running mean wind speed averaged over 10 minutes, $\bar{V}_{10}$, instantaneous wind direction, α, and running mean wind direction averaged over 10 minutes, $\bar{\alpha}_{10}$, for the two events. Fig. 3.4 shows the 10 minutes time history of instantaneous wind speed, V, running mean wind speed averaged over 30 seconds, $\bar{V}_{30s}$, and instantaneous wind direction. Both Figs. 3.3 and 3.4 were plotted centering the maximum instantaneous wind speed. The North is set as 0°azimuths in the wind direction measurement, while the East is 90°with subsequent values in the clockwise direction.

The first event occurred on April 04, 2019, and had a maximum instantaneous wind speed of 22.5 m/s. The G_{60}, G_{10}, and G_1 values calculated at the instant of maximum wind speed are 2.2, 1.95, and 1.2 respectively. The wind direction changed from approximately 0 to 90°in about 20 minutes. The wind was mainly coming from the sea during the 10 minutes period shown in Fig. 3.4. The presence of significant wind before the occurrence of the ramp-up of the downburst is due to a background ABL wind that has been present starting a couple of days before this event. After the ramp down of the wind speed, the ABL wind speed before the ramp up was not maintained.

The second event occurred on October 02, 2019, and had a maximum instantaneous wind speed of 20.5 m/s. The G_{60}, G_{10}, and G_1 values calculated at the instant of maximum wind speed are 3.65, 2.34 and 1.26 respectively. From Fig. 3.4 it can be observed that the wind speed increased significantly from approximately 2 m/s to 20.5 m/s in 10 minutes. In addition, there is

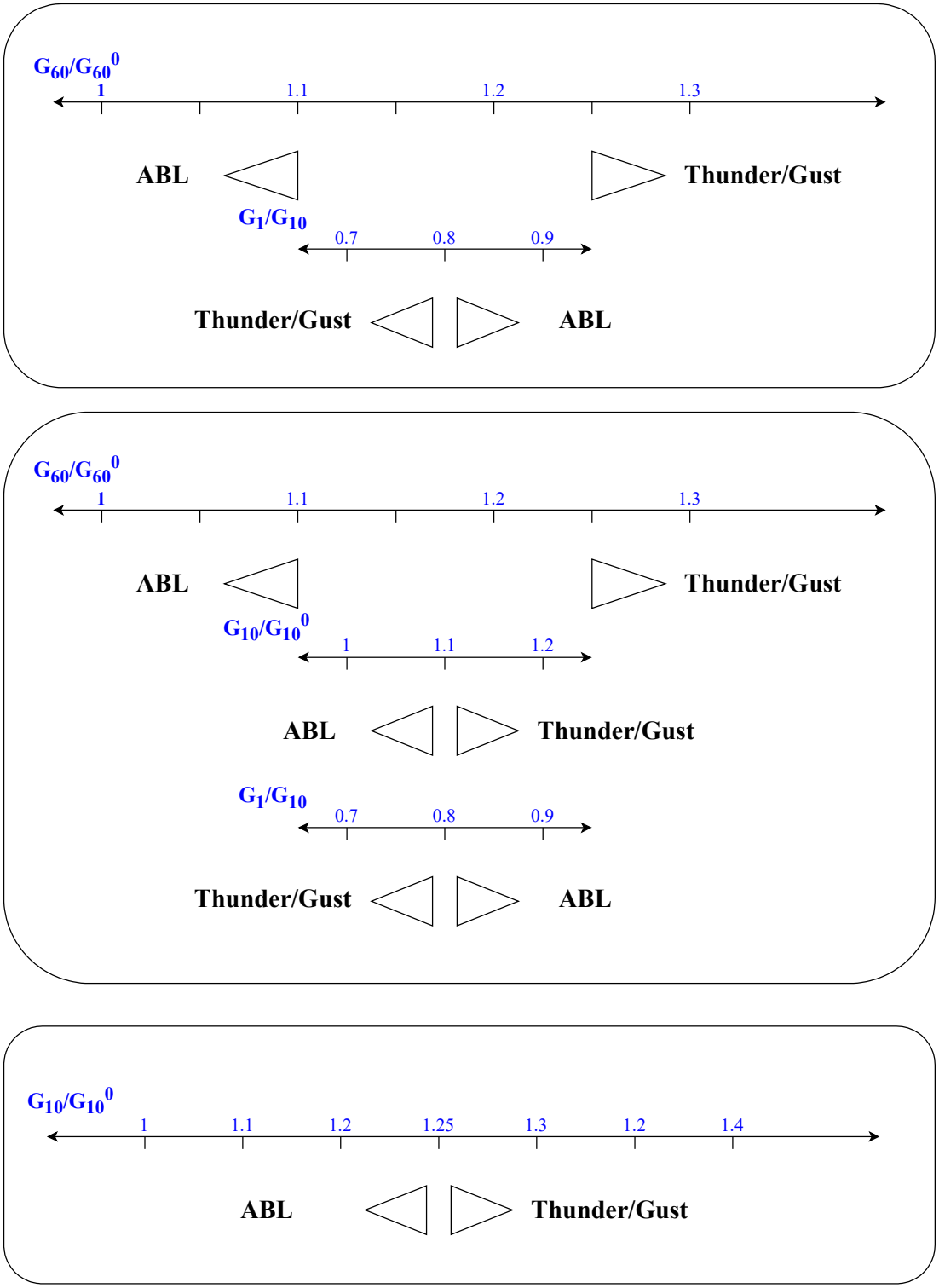

Fig. 3.2 Events separation process and threshold

Table 3.1 Gust factor ratios calculated at time instant of maximum wind speed

Event	G_{60}	G_{10}	G_1	$\frac{G_{60}}{G_{60}^0}$	$\frac{G_{10}}{G_{10}^0}$	$\frac{G_1}{G_{10}}$
April 04, 2019	2.21	1.95	1.24	1.39	1.3	0.63
Oct 02, 2019	3.65	2.34	1.26	2.3	1.56	0.34

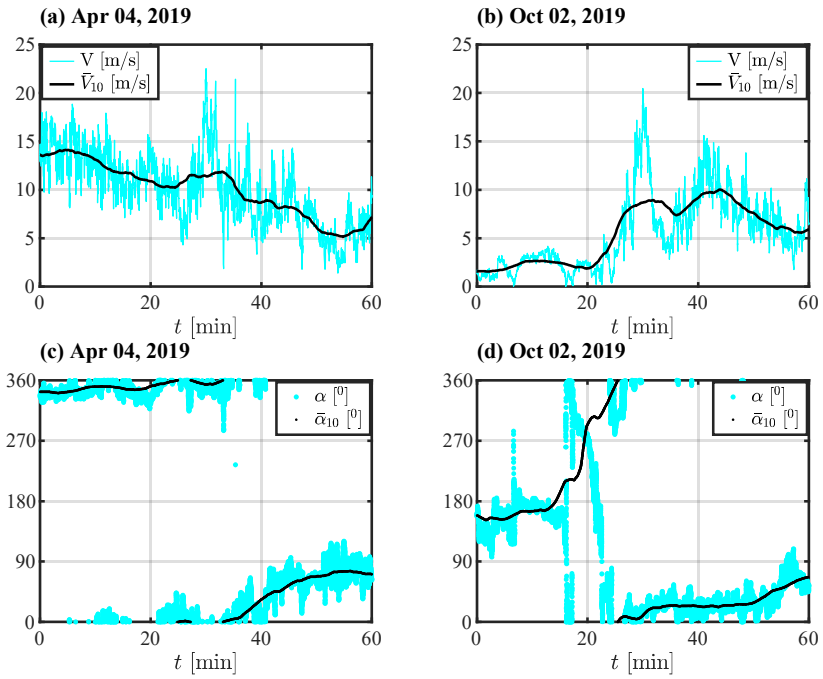

Fig. 3.3 1-hour time history of wind speed ((a) and (b)), and direction ((c) and (d)) centered at the maximum wind speed for the two downbursts

a significant change in wind direction of about 180°during the ramp-up of wind speed. Similar to the first event, the wind was mainly coming from the sea during the 10-minute period shown in Fig. 3.4.

The gust factors and normalized ratios calculated at the instant of maximum wind speed for the two selected downburst events are summarized in Table 3.1.

3.3.2 Decomposition of wind speed

Decomposition of horizontal wind speed into a mean and fluctuating component is a common procedure in synoptic winds to study the mean static and dynamic responses of structures separately. Similarly, studies on thunderstorm winds also decomposed wind speed into a slowly

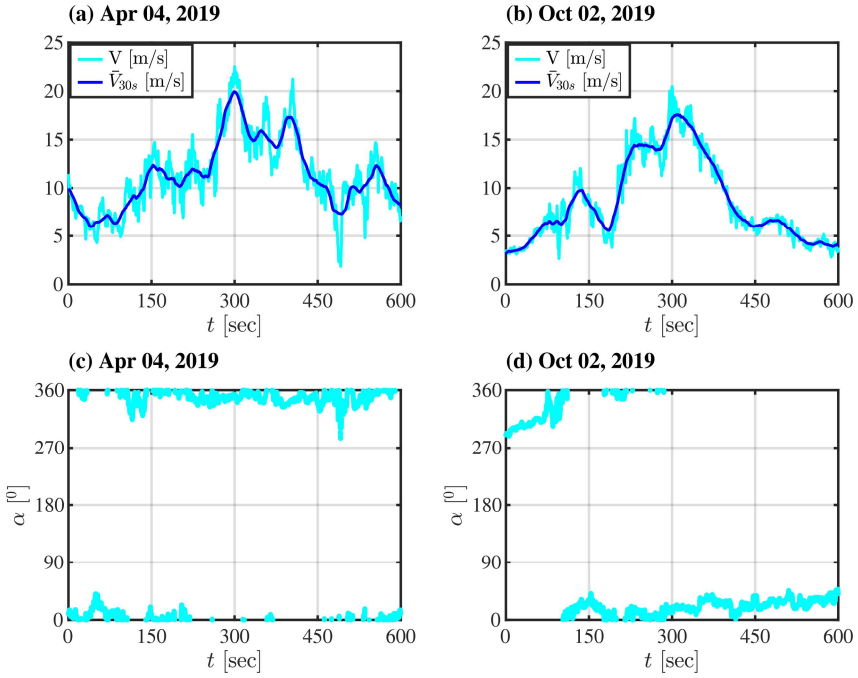

Fig. 3.4 10 minutes time history of wind speed ((a) and (b)), and direction ((c) and (d)) centered at the maximum wind speed for the two downbursts

varying mean and fluctuating component. Contrary to the classical approach in ABL winds, the decomposition approach applied for thunderstorm winds ignored the fluctuating component in the crosswind direction. Because of this, subsequent research on the dynamic response of structures to thunderstorm winds considered only the alongwind response and neglected the change in the angle of attack with time (Chen and Letchford, 2004; Choi and Tanurdjaja, 2002; Kwon and Kareem, 2009; Solari, 2016; Solari et al., 2015b, 2017). Zhang et al. (2019) proposed a new approach, referred to as directional decomposition, in which the wind speed is decomposed into slowly varying mean and fluctuating component in the alongwind direction, and fluctuating component in the crosswind direction. This enabled the estimation of alongwind and crosswind response and consideration of the change in the angle of attack (Brusco et al., 2019). Hence, this approach has been used to decompose wind speed for the two downburst events considered in this study.

Following the procedure defined in Solari et al. (2015a), a preliminary analysis has been made, to select the most convenient time averaging. In particular, the slowly varying mean was calculated using 10, 20, 30, and 40-second averaging windows and the frequency contents of the slowly varying mean and of the fluctuating components were evaluated. The results showed that, for the two considered events, 30 seconds is the average window that best separates the two harmonic contents, so it was used for this study.

The directional decomposition technique is illustrated in Fig. 3.5. First, slowly varying mean wind speeds averaged over 30 seconds, $\bar{V}_E(t)$ and $\bar{V}_N(t)$, are extracted from the instantaneous wind speed registered in the East and North directions, $V_E(t)$ and $V_N(t)$, respectively. The residues after the extraction of the mean are the fluctuating components, V'_E and V'_N.

$$V_E(t) = \bar{V}_E(t) + V'_E(t) \tag{3.2}$$

$$V_N(t) = \bar{V}_N(t) + V'_N(t) \tag{3.3}$$

The mean wind speed components, $\bar{V}_E$ and $\bar{V}_N$, are vector summed to obtain the resultant slowly varying mean wind speed, $\bar{u}(t)$, and its direction, $\bar{\beta}(t)$.

$$\bar{u}(t) = \sqrt{\bar{V}_E^2(t) + \bar{V}_N^2(t)} \tag{3.4}$$

$$\bar{\beta}(t) = \arctan 2\left[\frac{\bar{V}_N(t)}{\bar{V}_E(t)}\right] \tag{3.5}$$

The remaining fluctuating components, $V'_E(t)$ and $V'_N(t)$, are projected on new orthogonal axes, x-y, in which the x-axis is aligned with $\bar{u}(t)$.

$$u'(t) = V'_E(t)\cos\bar{\beta}(t) + V'_N(t)\sin\bar{\beta}(t) \tag{3.6}$$

$$v'(t) = -V'_E(t)\sin\bar{\beta}(t) + V'_N(t)\cos\bar{\beta}(t) \tag{3.7}$$

The alongwind and crosswind fluctuating components, $u'(t)$ and $v'(t)$, are further decomposed as a product of their standard deviation, $\sigma_u(t)$ and $\sigma_v(t)$, and rapidly varying stationary-Gaussian components, $\tilde{u}'(t)$ and $\tilde{v}'(t)$.

$$u'(t) = \sigma_u(t)\,\tilde{u}'(t) \tag{3.8}$$

$$v'(t) = \sigma_v(t)\,\tilde{v}'(t) \tag{3.9}$$

Thus, the alongwind and crosswind components of the wind speed are expressed as:

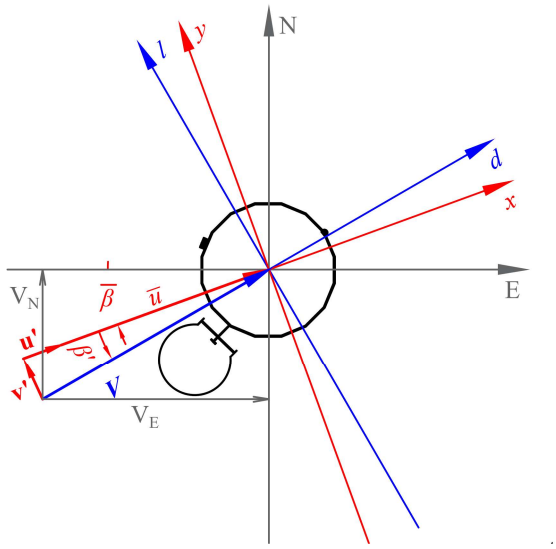

Fig. 3.5 Directional decomposition of wind speed

Table 3.2 Main features of wind speed for the two events

Event	$\bar{u}(t)_{\max}$ (m/s)	$\sigma_u(t)_{\max}$ (m/s)	$\sigma_v(t)_{\max}$ (m/s)	$I_u(t)_{mean}$ (-)	$I_v(t)_{mean}$ (-)
April 04, 2019	19.9	2.64	2.6	0.13	0.11
Oct 02, 2019	17.6	1.69	1.59	0.09	0.09

$$u(t) = \bar{u}(t) + u'(t) = \bar{u}(t)\left[1 + I_u(t)\,\tilde{u}'(t)\right] \tag{3.10}$$

$$v(t) = v'(t) = \bar{u}(t)\,I_v(t)\,\tilde{v}'(t) \tag{3.11}$$

where $I_u(t) = \sigma_u(t)/\bar{u}(t)$ and $I_v(t) = \sigma_v(t)/\bar{u}(t)$ are the longitudinal and lateral slowly varying turbulence intensities. $u(t)$ and $v(t)$ can be vector summed to get the resultant wind speed $V(t)$ which results in drag and lift forces parallel and perpendicular to it, along instantaneous aerodynamic axes d-l shown in Fig. 3.5.

Figs. 3.6 and 3.7 show the 10-minute time history of components of wind speed and wind direction obtained through directional decomposition for the two case studies. The 10-minute time history is extracted centering the time instant at which the resultant wind speed is maximum. The main features of the wind speed components are summarized in Table 3.2.

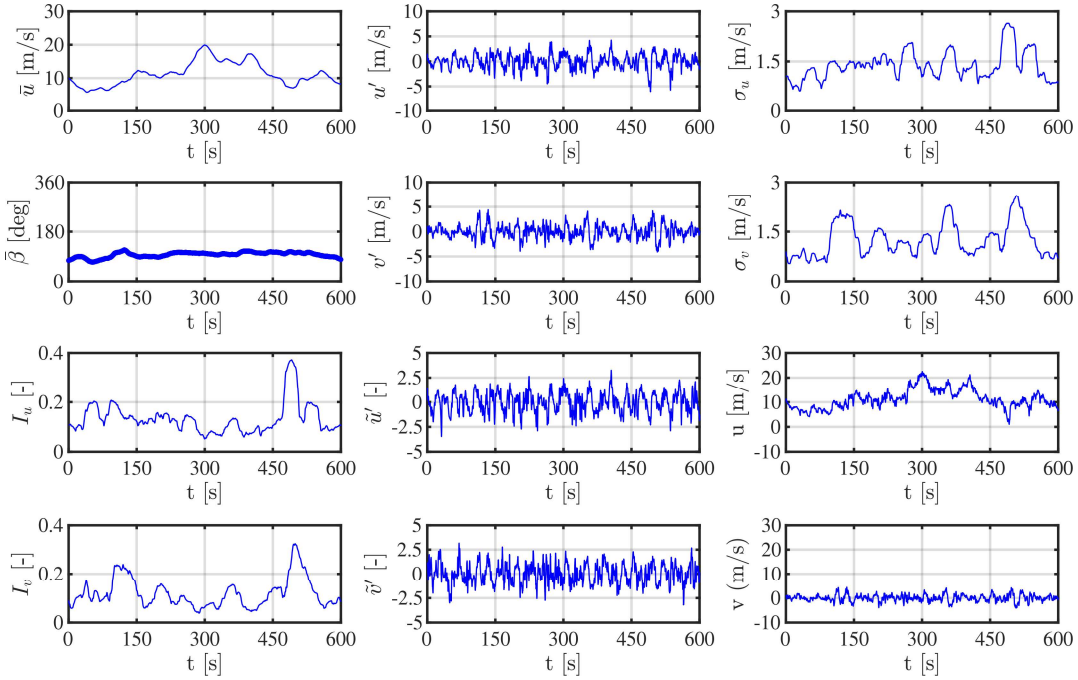

Fig. 3.6 Decomposition of wind speed for the downburst event on Apr 04, 2019

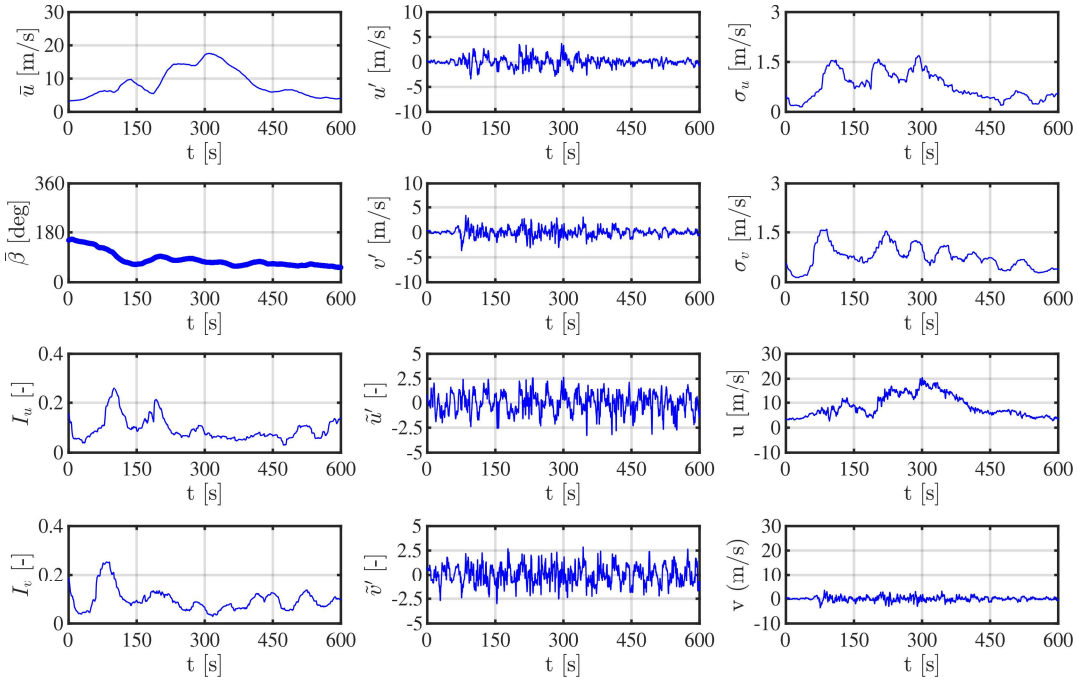

Fig. 3.7 Decomposition of wind speed for the downburst event on Oct 02, 2019

3.3.3 Top displacement from strain

Although the monitoring station is equipped with both accelerometers and strain gauges, the strain gauge readings were better at capturing the response because both the quasi-steady and resonant components of the response can be obtained from the strain gauge readings while the quasi-steady part of the response is unreliable in the accelerometer readings. This is because of the inherent properties of strain gauges and accelerometers, where the strain gauges register the strain due to both the low and high-frequency vibrations while the accelerometers do not register the low-frequency component of the vibration. Thus, part of the low-frequency component of the quasi-steady vibration is lost in the acceleration registrations.

Initially, the strain gauge readings had to be calibrated to have a zero-strain measurement when there is no wind load exerted on the structure. The calibration had to be done for each event separately because of the inherent property of strain gauges, in which the resistance changes in time (long-term drift). For this calibration, the time instant, t_s, at which wind speed is almost zero in the previous 2 - 72 hours before the downburst event had to be found. Once this time instant, t_s, is found for both downbursts, the strain measurement of each strain gauge at t_s was identified as the strain shift. This strain shift was subtracted from each of the strain gauge readings, to obtain the correct strain value.

As shown in Fig. 2.2, there are 8 strain gauges registering strain at two different heights of the structure. Since strain due to axial load in the structure is not part of the registered strain, the strain gauge readings can safely be assumed to be the result of pure biaxial bending resulting from the lateral wind load. In addition, the two locations at which the strain gauges are attached to the surface of the structure, are below the vertical ladder attached to the pole and as a result, the cross-section is approximately polar symmetric. Thus, the strains measured by strain gauges installed on the opposite faces of the cross-section are expected to have a similar magnitude of tension and compression strain.

With the assumption of pure biaxial bending, the deflection of the structure from strain gauge readings can be obtained by applying the Bernoulli-Euler beam equation for small deflection:

$$\frac{d^2\delta(t,z)}{dz^2} = \frac{M(t,z)}{EI(z)} \tag{3.12}$$

where δ is deflection; z is height; M is bending moment; I is area moment of inertia; and E is elastic modulus.

From flexure theory, $M(t,z) = S(t,z)I(z)/r(z)$, where S is flexural stress and r is the distance from the centroid of the cross-section to the outermost point. Assuming the section to

be linearly elastic, Hook's law can be applied, and flexural stress can be expressed as a product of strain, $\varepsilon(t,z)$ and modulus of Elasticity, E .

$$M(t,z) = \frac{\varepsilon(t,z)\,EI(z)}{r(z)} \tag{3.13}$$

Assuming the defection to have resulted from only 1^{st} mode single curvature bending, it can be expressed as a product of the principal coordinate of deflection,$P_{1,i}$, and modal shape, $\psi_{1,i}(z)$.

$$\delta_i(t,z) = P_{1,i}(t)\,\psi_{1,i}(z) \qquad i = X,Y \tag{3.14}$$

Substituting Eq. (3.13) and Eq. (3.14) in Eq. (3.12),

$$P_{1,i} = \frac{\varepsilon(t,z)}{r(z)\frac{d^2\psi_{1,i}(z)}{dz^2}} \qquad i = X,Y \tag{3.15}$$

As discussed in Chapter 2, the structure is not polar symmetric and the first two modes are single curvature bending about the two orthogonal directions X and Y. Thus resultant deflection of the structure should be the vector sum of deflection in X and Y direction. To obtain the principal coordinate of deflection in the X and Y direction, first, strains at the outermost points of the cross-section in the two principal directions have to be calculated. These strains, ε'_A to ε'_H, were calculated from the available sets of strain measurements, ε_A to ε_H, assuming a linear strain distribution with zero strain at the centroid of the section and maximum strain at the outermost surface. In the strain registration, tensile strain is positive, and compressive strain is negative.

Using Eq. 3.15, strains, ε'_A , ε'_C , ε'_E , ε'_G, are used to calculate the principal coordinate of deflection in the X direction, $P_{1,X}(t)$, and strains, ε'_B, ε'_D, ε'_F, ε'_H, are used to calculate the principal coordinate of deflection in the Y direction, $P_{1,Y}(t)$.

$r(z)$ is 257.9 mm at $z = 0.5$ m from the base of the structure where strain gauges ε'_A to ε'_D are installed and $r(z)$ is 249.65 mm at $z = 1.5$ m from the base of the structure where strain gauges ε'_E to ε'_H are installed. Since the 1^{st} bending modal shape is approximated by a power function with exponent ζ, its second derivative is,

$$\frac{d^2\psi}{dz^2} = \zeta(\zeta-1)\left(\frac{z}{H}\right)^{\zeta-2}\frac{1}{H^2} \tag{3.16}$$

Figs. 3.8 and 3.9 show the time history of top displacements in the X and Y directions calculated using strains ε'_A to ε'_H for the two case studies of downbursts. Sub-figures (a) and (b) show the top displacements in the X and Y directions. Sub-figure (c) shows the polar plot of the

Table 3.3 Top displacement obtained from strain measurement

Event	Apr 04, 2019		Oct 02, 2019	
	mean	std	mean	std
$\bar{X}_{\max}$ (cm)	1.76	0.55	2.77	0.67
$\bar{Y}_{\max}$ (cm)	5.28	0.41	2.52	0.24
$X\prime_{\max}$ (cm)	2.97	0.78	2.31	0.61
$Y\prime_{\max}$ (cm)	4.27	0.37	2.36	0.20
$\sigma_{X\max}$ (cm)	0.98	0.26	0.83	0.22
$\sigma_{Y\max}$ (cm)	1.42	0.13	0.90	0.08

resultant displacement obtained using all the possible pairs of orthogonal strains. Sub-figures (d) and (e) show the running mean top displacements averaged over 30 seconds, $\bar{X}$ and $\bar{Y}$, that is extracted from the top displacement obtained using each strain record, X and Y. Sub-figures (f) and (g) show the residual fluctuating top displacements, X' and Y', that are obtained by subtracting the running mean top displacements, $\bar{X}$ and $\bar{Y}$, from the total top displacements, X and Y. Sub-figures (h) and (i) show the time-varying standard deviations of the fluctuating top displacements, σ_X and σ_Y, that are obtained by calculating the running standard deviations of the residual fluctuations over 30 seconds. Table 3.3 summarizes the ensemble mean values and standard deviations of the maximum top displacement parameters obtained using the eight strain gauges. Some variability of results obtained from different strain gauges can be observed. Although tracing the cause of these variabilities is not trivial, temperature-induced effects in strain measurement and strain calibration errors could be the sources of error. Ideally, only two strain gauges oriented on orthogonal faces of the cross-section could be sufficient to measure the response but the availability of 8 strain gauges enabled us to obtain 4 displacement results in each orthogonal direction. This will be useful in compensating for the variability observed among strain gauges through averaging.

3.3.4 Top displacement from acceleration

The monitored structure is equipped with accelerometers at two heights. The accelerometer at 10.5 m was working during both of the selected downburst events but the accelerometer at 16.6 m was not working during the downburst event on October 02, 2019. Although the accelerometer at 16.6 m is expected to have a better amplitude-to-noise ratio for the analysis of the first bending modes, an acceleration measurement at 10.5 m is also sufficient to derive the structural response for the first vibration modes in the two principal bending directions.

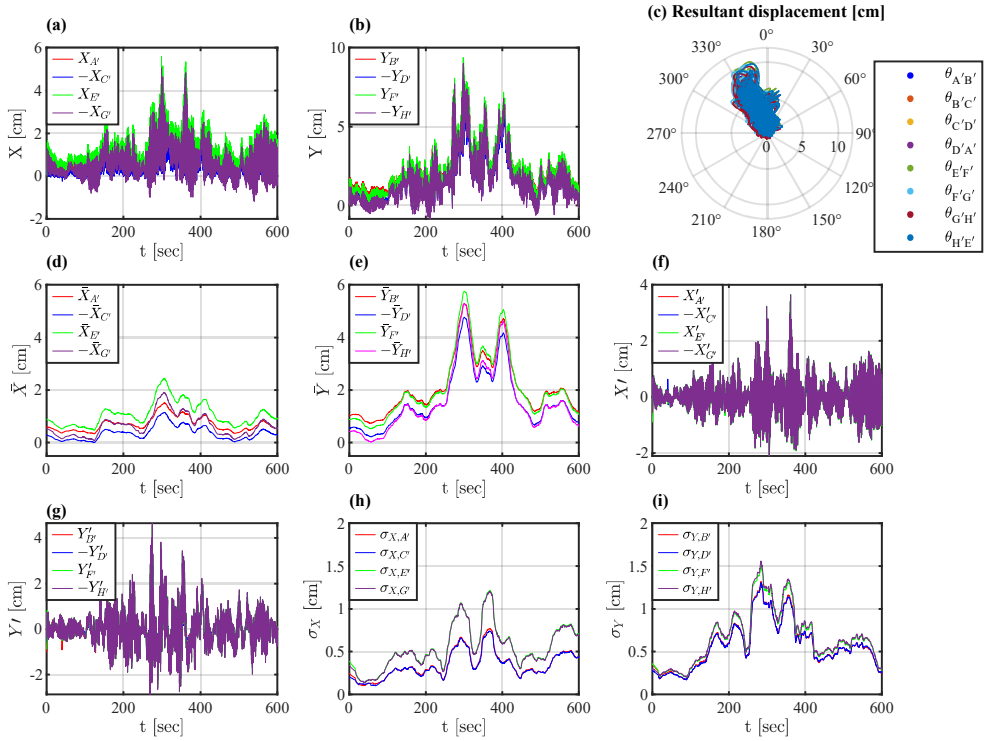

Fig. 3.8 Top displacement calculated using strain registrations ((a) and (b)), resultant (c), mean part ((d) and (e)), fluctuating part ((f) and (g)), and standard deviation of the fluctuating part ((h) and (i)) for the downburst on April 04, 2019

The high-frequency component of the response is expected to be satisfactorily registered by the accelerometers while the low-frequency quasi-steady component is expected to be erroneous due to the inherent property of the accelerometers. On the other hand, the strain gauges are expected to capture both the quasi-steady and resonant parts of the response. However, analysis of the acceleration measurement is important to validate the strain measurements and to check if all the important frequency components were captured by the strain gauges. Thus, the fluctuating component of displacement of the structure had to be calculated from the acceleration measurements and compared with the result obtained from strain gauges. The comparison was initially done in the frequency domain by plotting the PSD of displacement at 10.5 m obtained from strain measurement and the PSD of displacement at 10.5 m obtained through dividing the PSD of acceleration by ω^4, where ω is the circular frequency. Since the process is not stationary, the comparison was done carefully by calculating the PSD of both results considering similar segment length and overlapping through the Welch method. Fig. 3.10 shows a comparison made between the results of strain ε_A and ε_D with the results of acceleration A_{X2} and A_{Y2} for the two

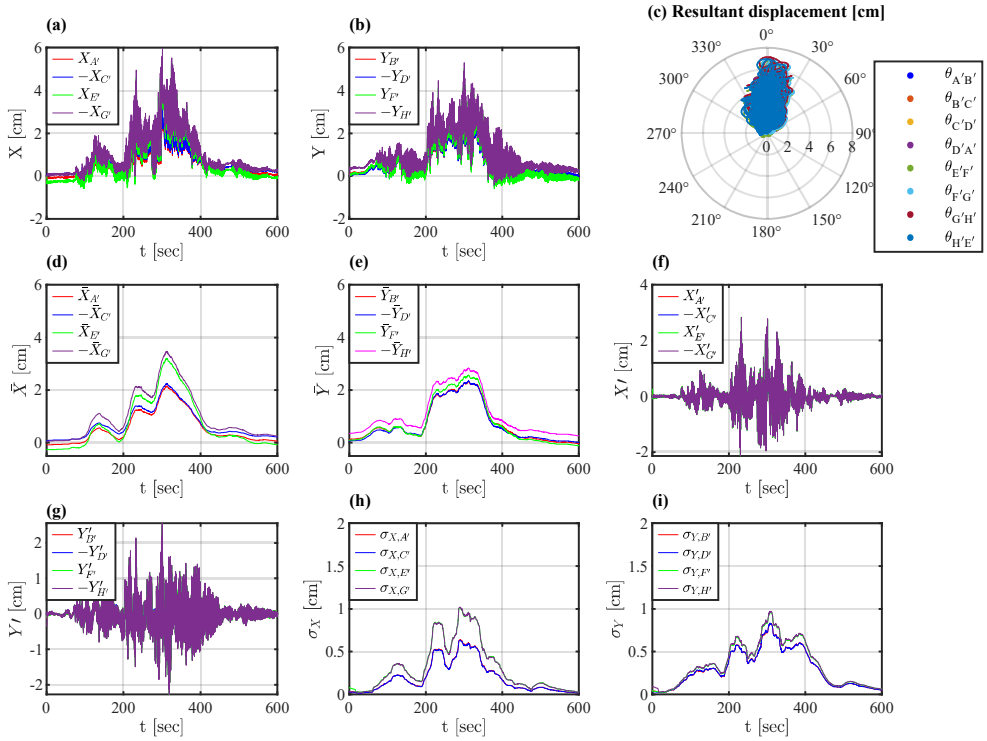

Fig. 3.9 Top displacement calculated using strain registrations ((a) and (b)), resultant (c), mean part ((d) and (e)), fluctuating part ((f) and (g)), and standard deviation of the fluctuating part ((h) and (i)) for the downburst on October 02, 2019

selected downburst events. As expected, the two results are not matching in the low-frequency region representing the quasi-steady response but the results are comparable near the first and second mode frequencies, 0.75 Hz and 0.85 Hz. In general, the results of acceleration appear to be slightly higher than the results of strain for the first two bending modes but the reverse is true for higher frequencies.

In theory, displacement can be calculated from acceleration through double integration. However, in reality, this calculation is not trivial because of the unknown initial conditions and the presence of noise. Integration of an acceleration measurement that has noise to obtain velocity or displacement usually results in a drift and this requires attention in numerical applications. In this study, a rigorous procedure was applied to avoid drift and minimize sources of errors. Initially, the acceleration measurement was bandpass filtered between 0.6 and 1 Hz to remove noise. Then, double integration was applied numerically to calculate the displacement. Finally, a high pass filter with a pass band frequency of 0.6 Hz was applied to remove the resulting drift. In Fig. 3.11, the displacement at 10.5 m obtained using strain gauges bandpass filtered between

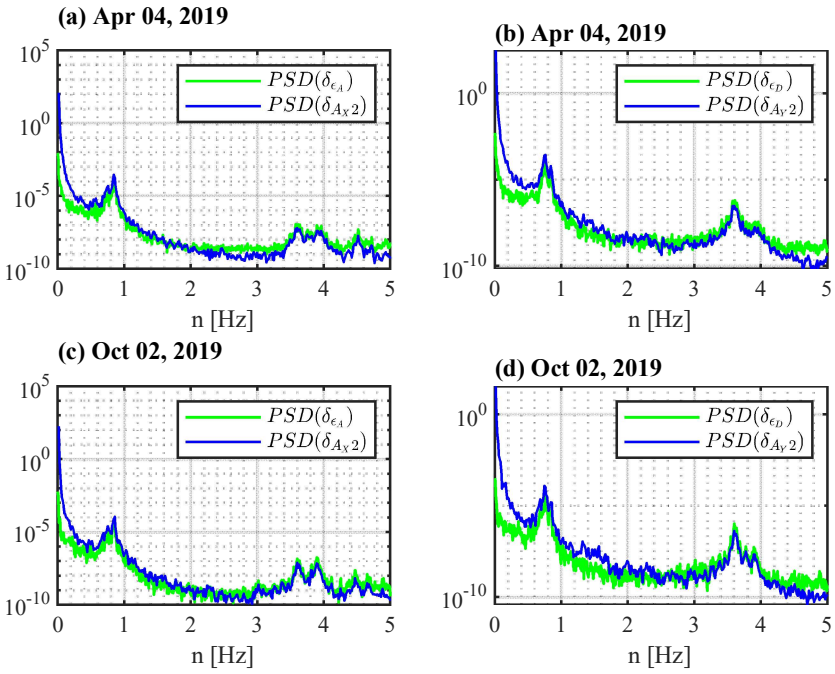

Fig. 3.10 PSD of displacement in the XX and YY direction at 11m obtained from strain and acceleration

frequencies of 0.6 and 1 Hz is compared with the displacement obtained from double integration of acceleration for strains and accelerations ε_A, ε_B, A_{X2}, and A_{Y2}. For better comparison, the running standard deviation of the displacement averaged over 30 seconds, σ_{XX} and σ_{YY} were calculated for displacement obtained from each strain gauge and acceleration. The result is presented in Fig. 3.12. Although the general trend of the time history of displacement fluctuation is similar, it can be noted that the displacement obtained from acceleration registrations is always higher than the one obtained from strain registrations. Possible causes of this discrepancy could be instrumentation or calibration error in either of the two measurements.

Considering the transient nature of downburst winds and response, the comparison between the top displacement obtained using strain and acceleration measurement was done in the time-frequency domain. Fig. 3.13 and 3.14 show the spectrograms of the top displacement obtained using strain and acceleration measurements in the two principal directions of the structure. In general, it can be observed that the acceleration measurement yielded a higher value of top displacement in all frequency ranges. There is no clear indication of the variability of the intensity difference between the results of strain and acceleration measurements in time for different ranges of frequencies.

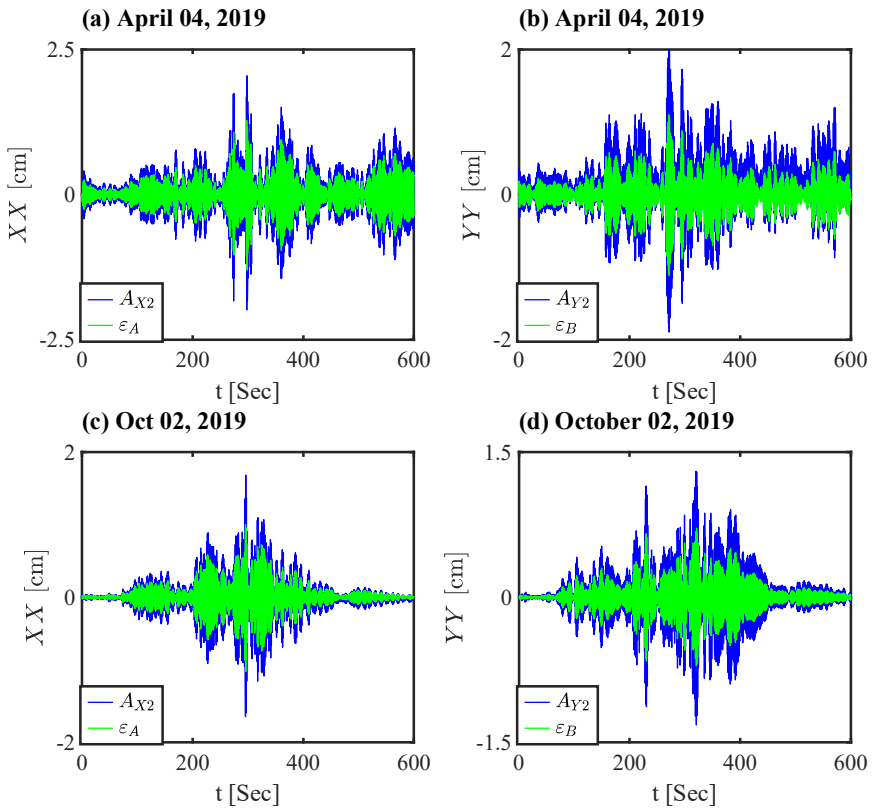

Fig. 3.11 Top displacement obtained from strain and acceleration

3.4 Discussion

3.4.1 Contribution of higher modes

In wind engineering, it is common to consider only the first few modes of vibration for the analysis of the dynamic amplification of displacement of the structure due to the turbulent wind. Similarly, in this study, only the first vibration modes in the two orthogonal principal bending directions are considered assuming the contribution of higher modes to be negligible. The contribution of higher modes was removed by lowpass filtering the strain gauge readings at a cutoff frequency of 1 Hz and by bandpass filtering the accelerometer readings between 0.6 and 1 Hz before the calculation of the structural displacement from strain and acceleration. To ensure that this assumption of negligible higher mode contribution is correct, a comparison between strain in the principal bending directions was made by separating the first mode and higher mode contributions through bandpass filtering. Fig. 3.15 shows an example of the comparison between the contribution of the first modes and the higher modes in the two principal bending directions

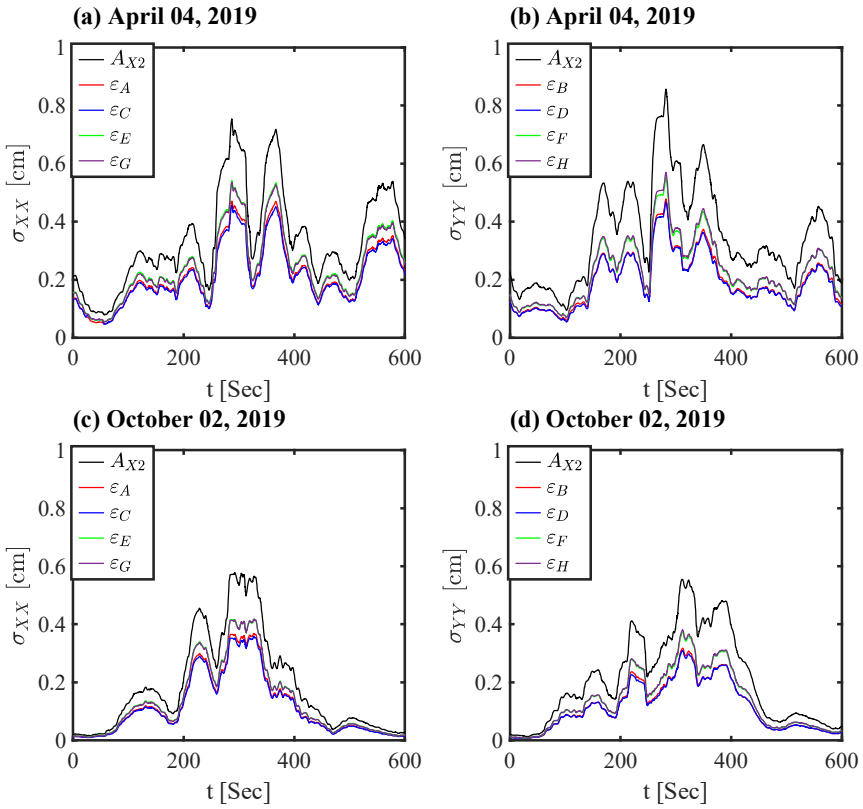

Fig. 3.12 The standard deviation of fluctuating top displacement obtained from strain and acceleration

on strain $\varepsilon_{A'}$ and $\varepsilon_{B'}$ during the two downburst events. Although the higher mode contribution is not entirely zero, it can be observed that the amplitude is not significant in comparison to the contribution of the first mode. The contribution of the first mode vibration was calculated by dividing the maximum strain obtained after applying a lowpass filter with a cutoff frequency of 1 Hz with the maximum strain obtained after applying a lowpass filter with a cutoff frequency of 10 Hz. The result is presented in Table 3.4 for each strain as a percentage. In all cases, the contribution of the first mode vibration was found to be more than 85%.

Table 3.4 Contribution of first mode vibration

Event	$\varepsilon_{A'}$	$\varepsilon_{B'}$	$\varepsilon_{C'}$	$\varepsilon_{D'}$	$\varepsilon_{E'}$	$\varepsilon_{F'}$	$\varepsilon_{G'}$	$\varepsilon_{H'}$
April 04, 2019	92.8%	87.9%	84.2%	90.6%	93.9%	92.6%	93.8%	92.6%
Oct 02, 2019	92.5%	86.6%	92.0%	86.8%	93.5%	87.7%	93.4%	88.0%

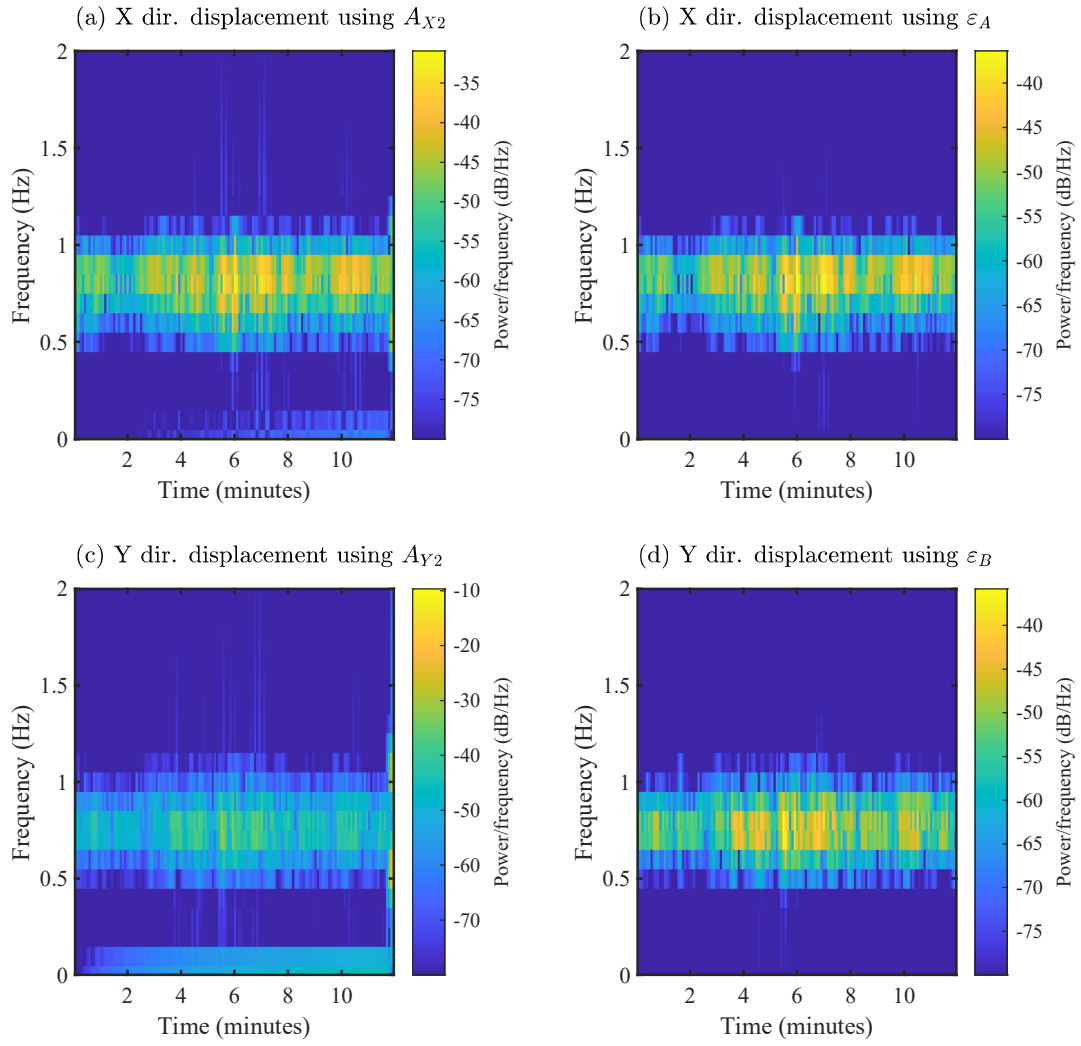

Fig. 3.13 The spectrograms of top displacement obtained using acceleration and strain measurements for the downburst event of April 04, 2019

3.4.2 Relationship between the fluctuation of the response and wind speed parameters

In this section, wind speed parameters such as time-varying mean wind speed and time-varying standard deviation of fluctuating wind defined in Section 3.3.2 are compared with simultaneous structural response parameters such as time-varying mean top displacement and time-varying standard deviation of the top displacement fluctuation presented in Section 3.3.3.

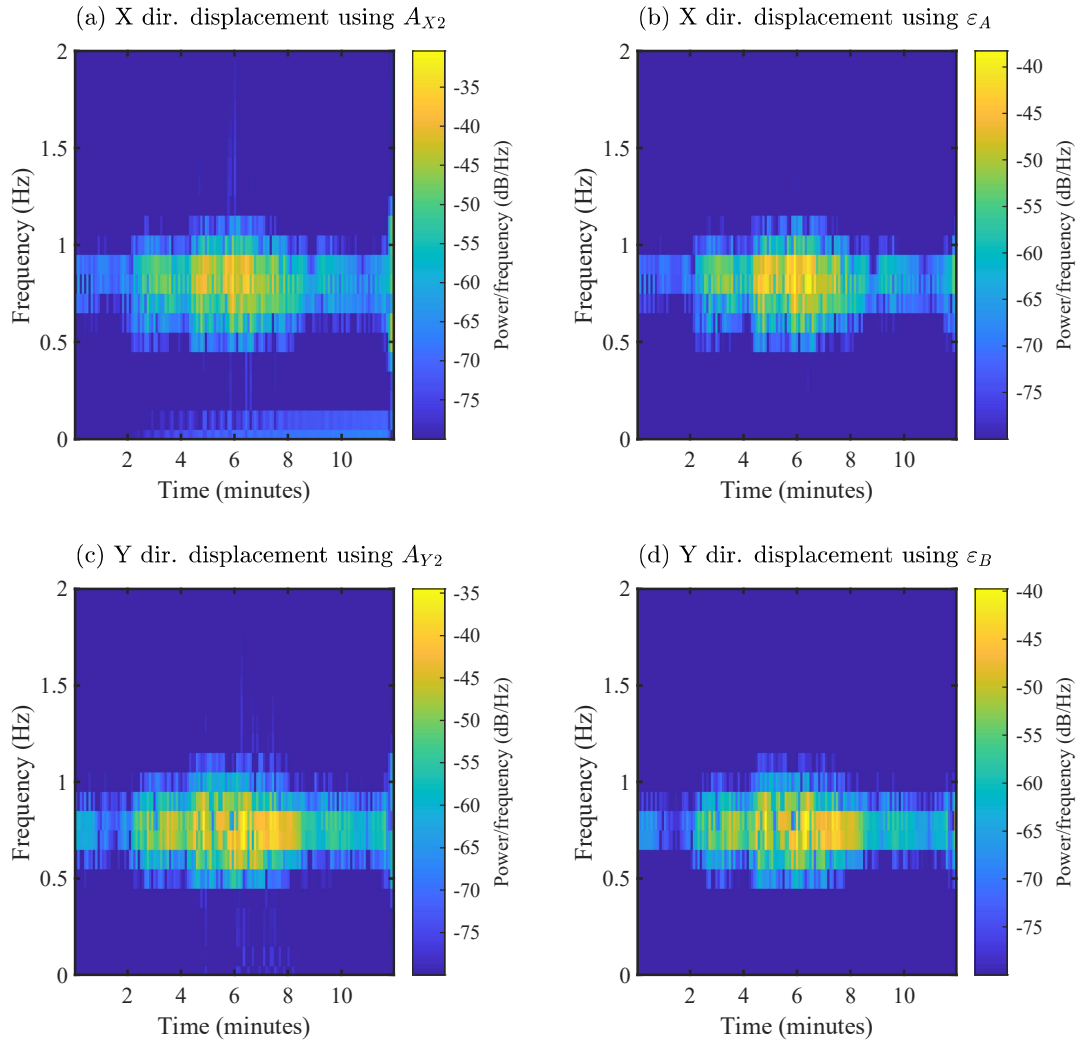

Fig. 3.14 The spectrograms of top displacement obtained using acceleration and strain measurements for the downburst event of October 02, 2019

The comparison is carried out between the time histories of the selected wind and structural response parameters by calculating their correlation coefficient. The calculated correlation coefficient, r, is reported on the top left/right corner of the time history plots for each of the comparisons and it is calculated as

$$r(A,B) = \frac{1}{N-1}\sum_{i=1}^{N}\left(\frac{A_i-\mu_A}{\sigma_A}\right)\left(\frac{B_i-\mu_B}{\sigma_B}\right) \tag{3.17}$$

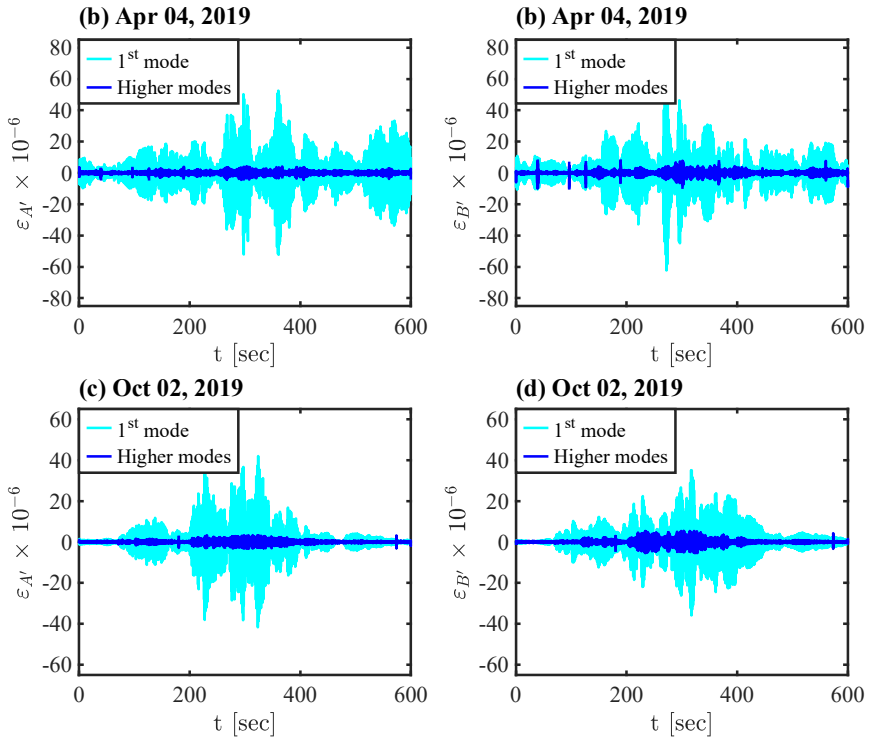

Fig. 3.15 Comparison between the contribution of 1^{st} mode and higher mode

where A and B are the two time series to be compared; μ_A and σ_A are the mean and standard deviation of A, respectively; μ_B and σ_B are the mean and standard deviation of B; and N is the number of data points.

Figs. 3.16 and 3.17 (a) and (b) show a plot of mean wind speed squared, $\bar{u}^2$ and mean top displacement in the alongwind and crosswind directions, $\bar{x}$ and $\bar{y}$. As can be observed from the similarity of the trend of the two plots and the value of the correlation coefficient, the alongwind response is closely correlated with the square of mean wind speed for both events. The trend of the time history of the crosswind top displacement also shows some resemblance with $\bar{u}^2$. This result is expected because, under the quasi-steady hypothesis, the aerodynamic force should be directly proportional to the square of the wind speed.

Figs. 3.16 and 3.17 (c) and (d) show a time history of mean wind speed squared, $\bar{u}^2$ and the standard deviation of the fluctuating top displacement in the alongwind and crosswind direction, σ_x and σ_y. In both cases, the maximum value of the standard deviation of the top displacement fluctuation is at the vicinity of the time instant at which the mean wind speed is maximum. In addition, the general trend of the standard deviation has some similarity with the trend of the

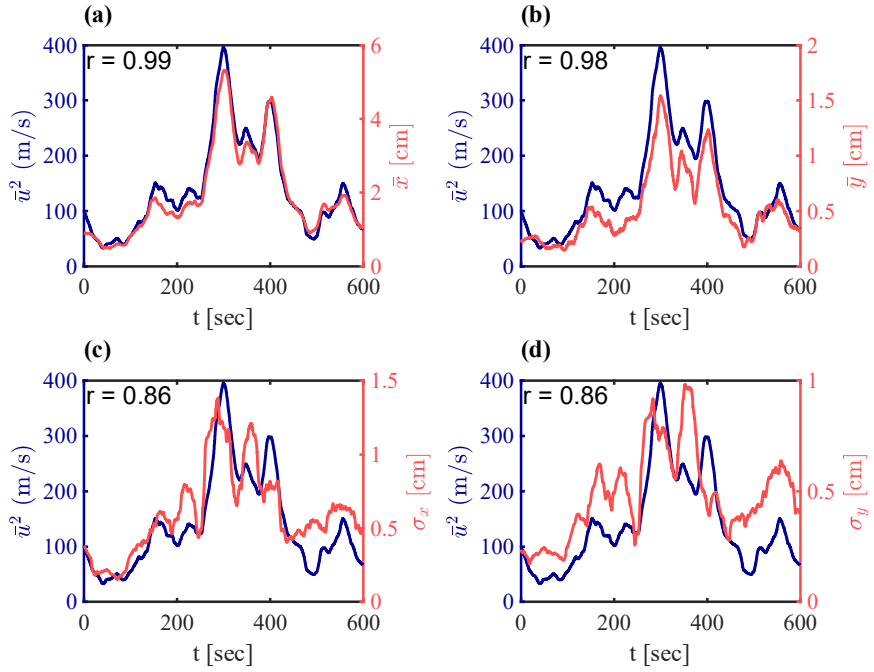

Fig. 3.16 Relationship between mean wind speed and top displacement for the event on April 04, 2019

square of the mean wind speed and they are positively correlated with a correlation coefficient of greater than 0.76.

Figures 3.18 and 3.19 show the time history of mean wind speed, $\bar{u}$, multiplied by the standard deviation of wind speed fluctuations, σ_u and σ_v, and standard deviation of the fluctuating top displacement, σ_x and σ_y in the alongwind and crosswind direction. This comparison is based on the quasi-steady theory, in which the fluctuating part of the response is made of two contributions; one proportional to $\bar{u}u'$ and one proportional to $\bar{u}v'$, whose respective weight depends on the aerodynamic coefficients (Piccardo and Solari, 2000). The results show that the alongwind response fluctuation is always highly correlated with $\bar{u}u'$ due to the weight of C_d with respect to the other coefficients. Regarding the crosswind response, the contributions of $\bar{u}u'$ and of $\bar{u}v'$ are more balanced due to the great variability of C_l and C_l'. However, the general high correlation values show the considerable contribution of all the aerodynamic coefficients (C_d, C_d', C_l, C_l') which, except for the drag coefficient are usually disregarded for polar symmetric structures.

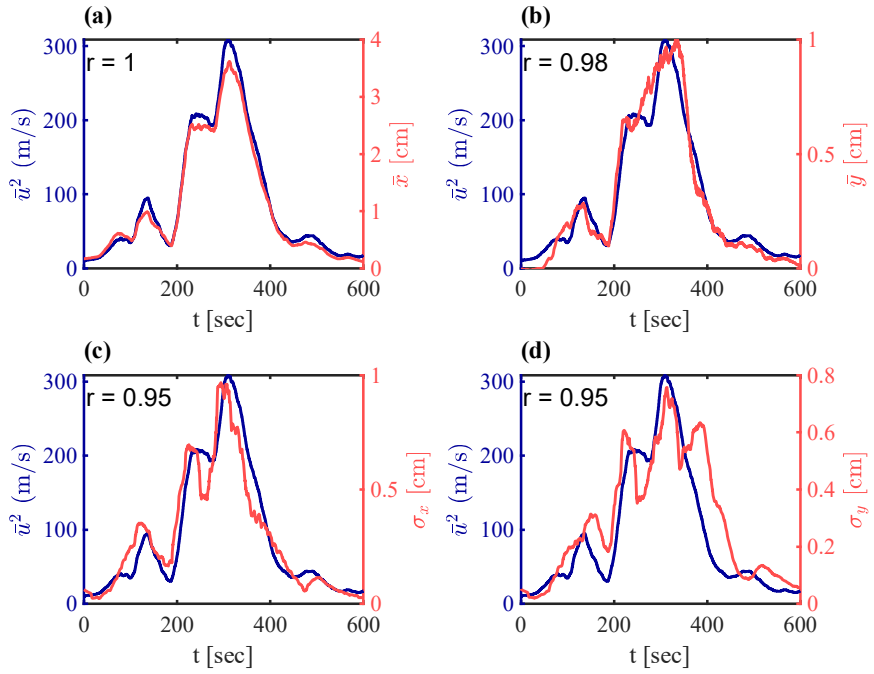

Fig. 3.17 Relationship between mean wind speed and top displacement for the event on October 02, 2019

3.4.3 Relationship between wind and response direction

The direction of the response of the structure is compared with the wind direction by calculating the direction of the response of the structure from displacements obtained using orthogonal strains. Fig. 3.20 (a) and (b) show a polar plot of the normalized mean wind speed, $\bar{u}$, and its direction, $\bar{\beta}$, as well as the normalized resultant mean top displacement and its direction. On the other hand, Fig. 3.20 (c) and (d) show the time history of mean wind direction and mean response direction. Comparing polar plots of mean wind speed and mean top displacement for the event on April 04, 2019, it is evident that the mean wind direction is approximately between 330 and 0 degrees but the response shows an approximate shift of 15 degrees towards the northwest direction relative to the mean wind direction. A similar shift of approximately 15 degrees can be visually observed for the event on October 02, 2019. The main cause for this shift in response relative to the wind direction could be the presence of lift force towards the southwest direction because of the presence of the attached ladder and intermediate platform on the southwest face of the pole.

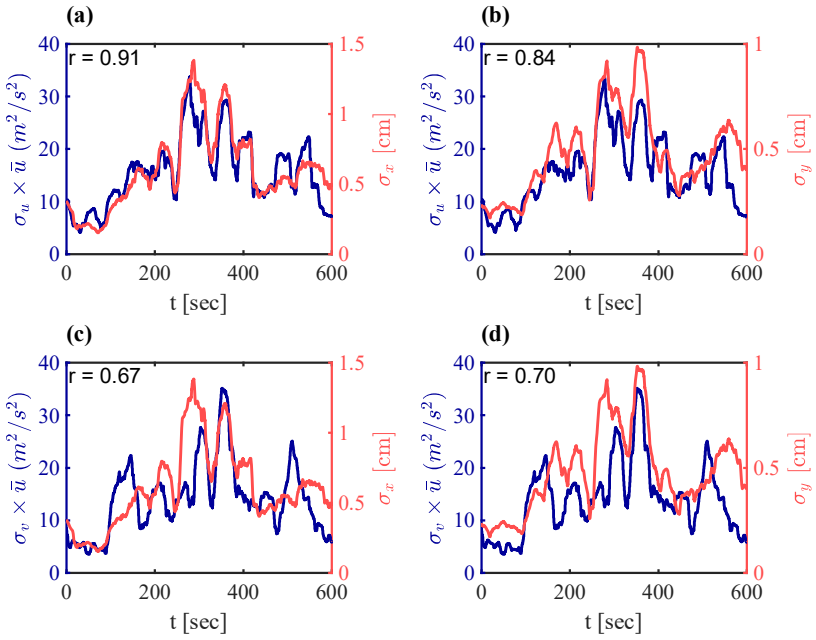

Fig. 3.18 Relationship between wind speed fluctuation and top displacement fluctuation for the event on April 04, 2019

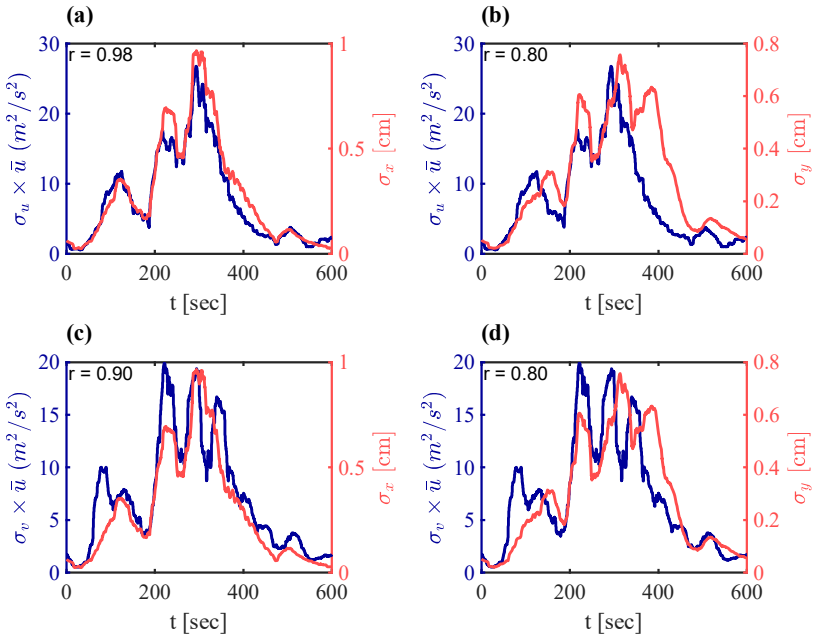

Fig. 3.19 Relationship between wind speed fluctuation and top displacement fluctuation for the event on October 02, 2019

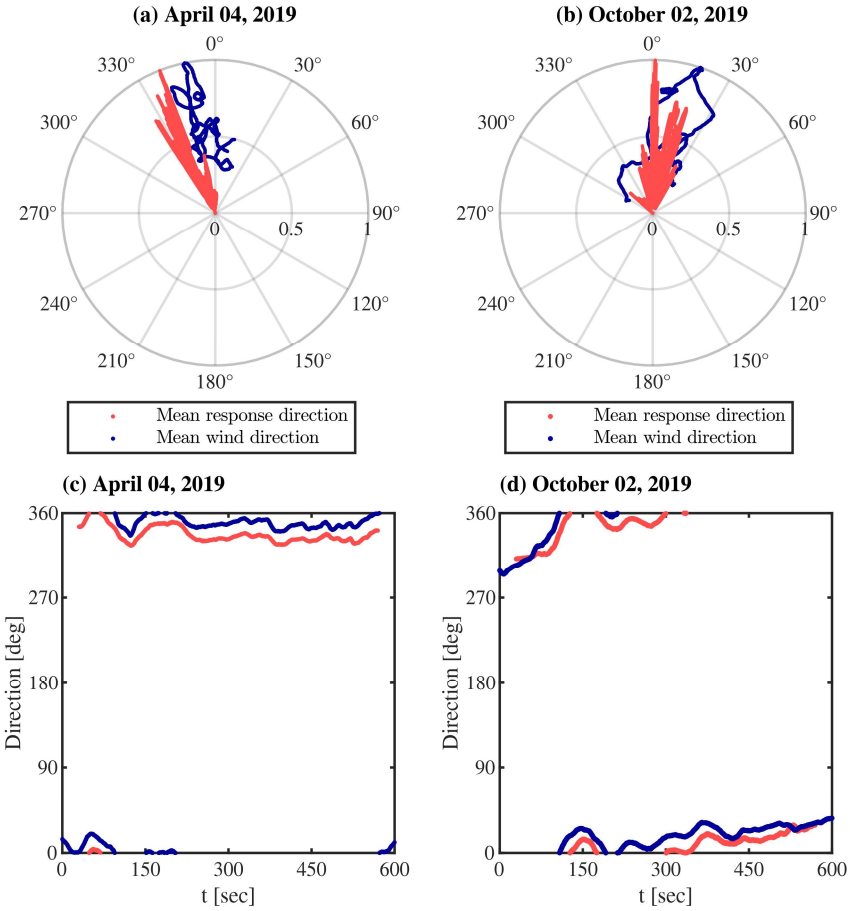

Fig. 3.20 Polar plot of normalized mean wind speed and normalized mean top displacement ((a) and (b)), and time history of mean wind direction and mean response direction ((c) and (d)) for the two downburst events

3.5 Conclusion

This study addressed the dynamic response of a slender lighting pole whose wind and structural response were monitored simultaneously with a long-term continuous monitoring system. Initially, an automatic algorithm was written for the separation of downburst and gust winds from depressions based on the wind speed measurement. The automatic algorithm was supplemented with qualitative judgment to separate downburst and gust winds. This enabled the selection of two case studies of downbursts whose wind and structural responses were registered by the monitoring system.

The time history of the displacement of the structure was estimated from the strain and acceleration measurements considering the first vibration modes of bending in the orthogonal directions. It was possible to obtain both the quasi-steady and resonant components of the displacement from strain measurements. This will be useful in future studies of the aerodynamics of similar structures under downburst winds. The contribution of higher modes of vibration was studied by separating the first vibration modes in the orthogonal bending directions modes from the rest of the vibration modes and comparing the maximum response in both cases. The contribution of higher modes was found to be less than 15% relative to the first bending modes. The relationship between the square of mean wind speed and the alongwind and crosswind displacement was studied and they were found to be highly correlated. The relationship between turbulence intensity and the standard deviation of the displacement fluctuation was also studied and they were found to be negatively correlated.

Because of the structural simplicity, availability of the structural properties, and availability of simultaneous measurement of wind and structural response for the two downburst case studies, this research will serve as one of the stepping stones toward validation of analytical downburst wind load calculation techniques through wind and structural response measurement. However, to extend the validation to the typical structures susceptible to downburst-induced damages, similar full-scale wind, and structural response monitoring are necessary for various groups of structures. Future monitoring stations might have to consider the installation of additional meteorological measurements such as temperature, atmospheric pressure, and relative humidity sensors on the monitored structures to facilitate the separation of downburst events from other gust fronts and ABL winds. Installation of anemometers at various heights of the structure is also highly recommended to enable the validation of the existing vertical profile of the mean wind speed and turbulent wind field models.

References

Aboshosha, H., Bitsuamlak, G., and El Damatty, A. (2015). Turbulence characterization of downbursts using LES. *J. Wind Eng. Ind. Aerodyn.*, 136:44–61.

Brusco, S., Lerzo, V., and Solari, G. (2019). Directional response of structures to thunderstorm outflows. *Meccanica*, 54(9):1281–1306.

Burlando, M., Zhang, S., and Solari, G. (2018). Monitoring, cataloguing, and weather scenarios of thunderstorm outflows in the northern Mediterranean. *Nat. Hazards Earth Syst. Sci.*, 18(9):2309–2330.

Chay, M. T., Albermani, F., and Wilson, R. (2006). Numerical and analytical simulation of downburst wind loads. *Eng. Struct.*, 28(2):240–254.

Chay, M. T. and Letchford, C. W. (2002). Pressure distributions on a cube in a simulated thunderstorm downburst—Part A: stationary downburst observations. *J. Wind Eng. Ind. Aerodyn.*, 90(7):711–732.

Chen, L. and Letchford, C. W. (2004). A deterministic-stochastic hybrid model of downbursts and its impact on a cantilevered structure. *Eng. Struct.*, 26(5):619–629.

Chen, X. (2008). Analysis of Alongwind Tall Building Response to Transient Nonstationary Winds. *J. Struct. Eng.*, 134(5):782–791.

Choi, E. C. and Hidayat, F. A. (2002). Gust factors for thunderstorm and non-thunderstorm winds. *J. Wind Eng. Ind. Aerodyn.*, 90:1683–1696.

Choi, E. C. and Tanurdjaja, A. (2002). Extreme wind studies in Singapore. An area with mixed weather system. *J. Wind Eng. Ind. Aerodyn.*, 90(12-15):1611–1630.

Cook, N. J., Ian Harris, R., and Whiting, R. (2003). Extreme wind speeds in mixed climates revisited. *J. Wind Eng. Ind. Aerodyn.*, 91(3):403–422.

De Gaetano, P., Repetto, M. P., Repetto, T., and Solari, G. (2014). Separation and classification of extreme wind events from anemometric records. *J. Wind Eng. Ind. Aerodyn.*, 126:132–143.

Durañona, V., Sterling, M., and Baker, C. J. (2007). An analysis of extreme non-synoptic winds. *J. Wind Eng. Ind. Aerodyn.*, 95(9-11):1007–1027.

Holmes, J., Forristall, G., and Mcconochie, J. (2005). Dynamic response of structures to thunderstorm winds. *10th Am. Conf. Wind Eng. ACWE 2005*, (July 2017).

Huang, G., Jiang, Y., Peng, L., Solari, G., Liao, H., and Li, M. (2019). Characteristics of intense winds in mountain area based on field measurement: Focusing on thunderstorm winds. *J. Wind Eng. Ind. Aerodyn.*, 190:166–182.

Junayed, C., Jubayer, C., Parvu, D., Romanic, D., and Hangan, H. (2019). Flow field dynamics of large-scale experimentally produced downburst flows. *J. Wind Eng. Ind. Aerodyn.*, 188(March):61–79.

Kim, J. and Hangan, H. (2007). Numerical simulations of impinging jets with application to downbursts. *J. Wind Eng. Ind. Aerodyn.*, 95(4):279–298.

Kwon, D. K. and Kareem, A. (2009). Gust-front factor: New framework for wind load effects on structures. *J. Struct. Eng.*, 135(6):717–732.

Letchford, C. W., Mans, C., and Chay, M. T. (2002). Thunderstorms - Their importance in wind engineering (a case for the next generation wind tunnel). *J. Wind Eng. Ind. Aerodyn.*, 90(12-15):1415–1433.

Lombardo, F. T., Main, J. A. M., and Simiu, E. (2009). Automated extraction and classification of thunderstorm and non-thunderstorm wind data for extreme-value analysis. *J. Wind Eng. Ind. Aerodyn.*, 97:120–131.

Mason, M. S., Letchford, C. W., and James, D. L. (2005). Pulsed wall jet simulation of a stationary thunderstorm downburst, Part A: Physical structure and flow field characterization. *J. Wind Eng. Ind. Aerodyn.*, 93(7):557–580.

Piccardo, G. and Solari, G. (2000). 3D Wind-excited response of slender structures: closed-form solution. *J. Struct. Eng.*, pages 936–943.

Repetto, M. P., Burlando, M., Solari, G., De Gaetano, P., and Pizzo, M. (2017). Integrated tools for improving the resilience of seaports under extreme wind events. *Sustain. Cities Soc.*, 32:277–294.

Romanic, D., LoTufo, J., and Hangan, H. (2019). Transient behavior in impinging jets in crossflow with application to downburst flows. *J. Wind Eng. Ind. Aerodyn.*, 184(November 2018):209–227.

Roncallo, L. and Solari, G. (2020). An evolutionary power spectral density model of thunderstorm outflows consistent with real-scale time-history records. *J. Wind Eng. Ind. Aerodyn.*, 203(April):104204.

Sengupta, A., Haan, F. L., Sarkar, P. P., and Balaramudu, V. (2008). Transient loads on buildings in microburst and tornado winds. *J. Wind Eng. Ind. Aerodyn.*, 96(10-11):2173–2187.

Solari, G. (1993). Gust buffeting. I: Peak wind velocity and equivalent pressure. *J. Struct. Eng.*, 119(2):365–382.

Solari, G. (2016). Thunderstorm response spectrum technique: Theory and applications. *Eng. Struct.*, 108:28–46.

Solari, G., Burlando, M., De Gaetano, P., and Repetto, M. P. (2015a). Characteristics of thunderstorms relevant to the wind loading of structures. *Wind Struct. An Int. J.*, 20(6):763–791.

Solari, G., Burlando, M., and Repetto, M. P. (2020). Detection, simulation, modelling and loading of thunderstorm outflows to design wind-safer and cost-efficient structures. *J. Wind Eng. Ind. Aerodyn.*, 200(January):104142.

Solari, G., De Gaetano, P., and Repetto, M. P. (2015b). Thunderstorm response spectrum: Fundamentals and case study. *J. Wind Eng. Ind. Aerodyn.*, 143:62–77.

Solari, G., Rainisio, D., and De Gaetano, P. (2017). Hybrid simulation of thunderstorm outflows and wind-excited response of structures. *Meccanica*, 52:3197–3220.

Twisdale, L. A. and Vickery, P. J. (1992). Research on thunderstorm wind design parameters. *J. Wind Eng. Ind. Aerodyn.*, 41(1-3):545–556.

Vermeire, B. C., Orf, L. G., and Savory, E. (2011). Improved modelling of downburst outflows for wind engineering applications using a cooling source approach. *J. Wind Eng. Ind. Aerodyn.*, 99(8):801–814.

Zhang, S., Solari, G., Burlando, M., and Yang, Q. (2019). Directional decomposition and properties of thunderstorm outflows. *J. Wind Eng. Ind. Aerodyn.*, 189(November 2018):71–90.